

Dynamical quantum phase transitions in a spinor Bose-Einstein condensate and criticality enhanced quantum sensing

Lu Zhou^{1,5,6,*}, Jia Kong³, Zhihao Lan^{4,†} and Weiping Zhang^{2,5,6‡}

¹State Key Laboratory of Precision Spectroscopy, Department of Physics, School of Physics and Electronic Science, East China Normal University, Shanghai 200241, China

²School of Physics and Astronomy, and Tsung-Dao Lee institute, Shanghai Jiao Tong University, Shanghai 200240, China

³Department of Physics, Hangzhou Dianzi University, Hangzhou 310018, China

⁴Department of Electronic and Electrical Engineering, University College London, Torrington Place, London WC1E 7JE, United Kingdom

⁵Shanghai Branch, Hefei National Laboratory, Shanghai 201315, China

⁶Collaborative Innovation Center of Extreme Optics, Shanxi University, Taiyuan, Shanxi 030006, China

Quantum phase transitions universally exist in the ground and excited states of quantum many-body systems, and they have a close relationship with the nonequilibrium dynamical phase transitions, which however are challenging to identify. In the system of spin-1 Bose-Einstein condensates, though dynamical phase transitions with correspondence to equilibrium phase transitions in the ground state and uppermost excited state have been probed, those taken place in intermediate excited states remain untouched in experiments thus far. Here we unravel that both the ground and excited-state quantum phase transitions in spinor condensates can be diagnosed with dynamical phase transitions. A connection between equilibrium phase transitions and nonequilibrium behaviors of the system is disclosed in terms of the quantum Fisher information. We also demonstrate that near the critical points parameter estimation beyond standard quantum limit can be implemented. This work not only advances the exploration of excited-state quantum phase transitions via a scheme that can immediately be applied to a broad class of few-mode quantum systems, but also provides new perspective on the relationship between quantum criticality and quantum enhanced sensing.

Introduction.—In quantum many-body systems, excited-state quantum phase transitions (ESQPTs) can be more appealing compared with quantum phase transitions (QPTs), which refer to quantum criticality aroused in ground states [1]. ESQPTs extend the study of criticality to excitation spectra and have recently been disclosed in several quantum systems [2–7]. The criticalities associated with QPTs and ESQPTs can reveal themselves by nonequilibrium quantum phenomena, especially dynamical phase transition (DPT) [8–19].

DPT is characteristic of the nonanalyticity in the Loschmidt echo rate function after quantum quench. More experimentally accessible clue would be that physical quantities become nonanalytical as a function of time, such as the order parameter. It is still an open question on the universal correspondence between DPTs and QPTs, also ESQPTs.

In this work, taking the system of an antiferromagnetic spin-1 Bose-Einstein condensate (BEC) as an example, we illustrate the relationship between DPTs and equilibrium phase transitions. Superfluidity and magnetism are simultaneously achieved in a spinor BEC. Due to the interplay between intrinsic spin-dependent collision interactions and Zeeman energy splittings controlled by an external field, the system of a spinor condensate features a rich phase diagram both in the ground and excited states [20–22]. QPTs have been experimentally explored in the ground state of spin-1 condensates with ferromagnetic [23] or antiferromagnetic [24–26] interaction, which show interesting phenomena and applications, such as, nontrivial dynamics in space [27, 28], Kibble-Zurek mechanism [29, 30], preparation of macroscopic many-body entangled state [31] and surpassing the standard quantum limit (SQL) [32]. The authors in [33] showed that the phase tran-

sition points can be mapped out through DPT with measurement on the long-time average of fractional population, which was used to explore the ESQPT taken place in the uppermost energy level [34]. However, little efforts have been devoted to the study of ESQPTs in the intermediate excited states until recently, a topological order parameter was proposed to characterize ESQPTs in a spinor BEC [35], whose measurement relies on the precise operation after one period of spin oscillation and thus can be experimentally challenging. Besides that, a mimic of ESQPTs in spinor condensates has also been studied in Raman-dressed spin-orbit coupled BECs [36, 37].

Though diverging oscillation periods [38] and winding number changing [33] are regarded to be linked to ESQPTs, they can also be explained within mean-field theory and an unambiguous quantum signature of ESQPTs has not been identified to our knowledge. On the other hand, only recently has the spin singlet (S) ground state been experimentally prepared and observed in an antiferromagnetic spinor BEC [39], since its first prediction in the 90s [40]. It is interesting to explore the DPTs between the S state and other ground states. Here, we show that both the QPTs and ESQPTs can be captured with DPT. Specifically, the nonequilibrium dynamics of DPT could be characterized by the quantum Fisher information (QFI), which are intimately related to Loschmidt echoes [41–45]. The prospect of quantum enhanced sensing with DPTs is also addressed.

QPTs and ESQPTs in an antiferromagnetic spin-1 condensate.—We consider a spinor BEC of N atoms with hyperfine spin $F = 1$. Within the single-mode approximation, which enables the internal spin dynamics being isolated from the external center-of-mass motion, the system is governed by

the Hamiltonian ($\hbar = 1$) [21, 22]

$$\hat{H} = \frac{c}{2N} \hat{S}^2 - q \hat{N}_0, \quad (1)$$

where c and q characterize the inter-spin and effective quadratic Zeeman energies, respectively. Here, $\hat{S}_{i=x,y,z} = \hat{a}_\alpha^\dagger S_i^{\alpha\beta} \hat{a}_\beta$ are spin-1 vector operators with \hat{a}_m (\hat{a}_m^\dagger) the bosonic annihilation (creation) operators for the magnetic sublevels $m = 0, \pm 1$ and $S_{i=x,y,z}$ the spin-1 matrices (the indices α, β are summed over m). The atom number operators $\hat{N}_m = \hat{a}_m^\dagger \hat{a}_m$ and $N = \sum_m \hat{N}_m$. While q can only take positive value if it is induced by an external magnetic field B , i.e., $q \propto B^2$, it can be tuned to both positive and negative values via microwave dressing [38, 46, 47]. In the following, we will concentrate on the antiferromagnetic spinor condensate ($c > 0$) with zero magnetization (note that the methods described here can be generalized to the cases of ferromagnetic condensate and finite magnetization).

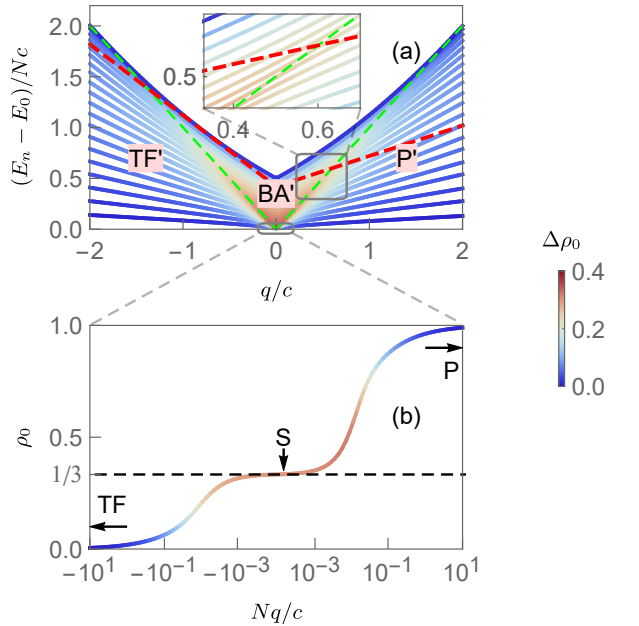


FIG. 1: Quantum phases of an antiferromagnetic spin-1 BEC of $N = 300$ atoms with zero magnetization, using the number variance $\Delta\rho_0$ in spin-0 component. (a) Excited spectra with every 15 eigenvalues. The green-dashed lines are the ESQPT lines. The red-dashed lines represent the mean-field energy \mathcal{E} of a CSS (4) with $\rho_0 = 0.7$. (b) Ground state varies with q from TF, S to P.

A sketch of the system phase diagram is given in Fig. 1, which is obtained via exact diagonalization of Hamiltonian (1) with an atom number $N = 300$. It will be helpful to rewrite Hamiltonian (1) in a more generic form as $\hat{H} = \hat{H}_0 + q\hat{H}_q$, and ground state properties can be recognized as results aroused by the competition between \hat{H}_0 and \hat{H}_q : (i) For $|q| \gg c$, the ground state is dominated by $\hat{H}_q = \hat{N}_0$, thus resulting in Polar (P) state and Twin-Fock (TF) state, with $\rho_0 \equiv \frac{\langle \hat{N}_0 \rangle}{N} = 1$ and 0 respectively, in the positive and negative

q direction, associated with vanishing variance $\Delta\rho_0 \equiv \frac{\Delta\hat{N}_0}{N}$; (ii) $\hat{H}_0 \propto \hat{S}^2$ restores SO(3) symmetry in a narrow window of $|q| < \frac{c}{N^2}$, resulting in S ground state with $S = 0$ for even N . State S is massively entangled typical of large variance $\Delta\rho_0$, and with atoms evenly distributed among the magnetic sublevels, representing a three-fragment mesoscopic quantum state with $\rho_0 = \frac{1}{3}$. In the thermodynamical limit (TL) of $N \rightarrow \infty$, the S state disappears and the QPT is characterized by a 1st-order phase transition between the P and TF state.

The excited eigenspectra display a cumulation of avoided crossings along $E = E_g + |q|$ (green-dashed lines in Fig. 1(a), see the inset for an enlarged view), which correspond to singularities in the density of states under TL. Thus we refer the lines as the ESQPT lines and the variances $\Delta\rho_0$ of the eigenstates in the vicinity of these lines also achieve maximum values. The three phases separated by these lines are labeled as P', TF' and BA' (broken-axisymmetry). While P' and TF' are named according to the corresponding ground states, BA' is named after the highest energy BA state [23, 48], which possesses a transverse magnetization perpendicular to the applied external field and thus breaks the SO(2) axisymmetry.

DPT and the QFI.— To explore the relation with equilibrium phase transitions, we characterize DPTs with the QFI, which is defined as the fidelity susceptibility [49–51]

$$F_Q(q, t) = -4 \frac{\partial^2 F(q, \delta q, t)}{\partial (\delta q)^2} \Big|_{\delta q \rightarrow 0}, \quad (2)$$

where the fidelity $F(q, \delta q, t) \equiv |\langle \psi(q, t) | \psi(q + \delta q, t) \rangle| = |\langle \psi_0 | e^{i\hat{H}(q)t} e^{-i\hat{H}(q+\delta q)t} | \psi_0 \rangle|$ is actually the Loschmidt echo, and it measures the revival of a state $|\psi_0\rangle$ experiencing time forward propagation under $\hat{H}(q)$ followed by reversed evolution with $\hat{H}(q + \delta q)$. One can expect that when the system becomes critical with $q \rightarrow q_c$, the quantum state evolution behaves singularly and exhibits quite distinct results even for a small δq , resulting in prominent decrease of the fidelity and a high F_Q . An approximate long-time secular analytic expression for the QFI can be found as [52]

$$F_Q(q, t) \simeq 4t^2 \left[\sum_n |c_n|^2 (H_q^n)^2 - \left(\sum_n |c_n|^2 H_q^n \right)^2 \right], \quad (3)$$

where $c_n = \langle \psi_n | \psi_0 \rangle$ is the projection of the initial state $|\psi_0\rangle$ onto the eigenstates $|\psi_n\rangle$ of the Hamiltonian (1), and $H_q^n = \langle \psi_n | \hat{H}_q | \psi_n \rangle$. Equation (3) indicates that a peak in the QFI can be attributed to either enhanced fluctuations in the order parameter ($H_q^n = N_0^n = \langle \psi_n | \hat{N}_0 | \psi_n \rangle$), or those in the overlaps between the initial state and the eigenstates.

To achieve the correspondence between DPTs and equilibrium phase transitions, one would expect that the overlap between the initial state and system eigenstates $|c_n|^2$ has similar singular distribution as the order parameter around the energy E_n^c . We propose to use coherent spin state (CSS) $|\zeta\rangle^{\otimes N}$ as the initial state, with $|\zeta\rangle \equiv \sum_m \zeta_m |m\rangle$ and $\zeta = \left(\sqrt{\frac{1-\rho_0+\rho_m}{2}} e^{i\chi_+}, \sqrt{\rho_0}, \sqrt{\frac{1-\rho_0-\rho_m}{2}} e^{i\chi_-} \right)$, where

$\rho_m = \frac{N_1 - N_{-1}}{N}$, $\chi_{\pm} = \frac{\theta_s \pm \theta_m}{2}$ with $\theta_{s(m)}$ the spinor phase and magnetization phase respectively. CSS can be visualized by casting the corresponding mean-field phase diagram at different q into the spin-nematic phase sphere $\{S_{\perp}, Q_{\perp}, 2\rho_0 - 1\}$ with the transverse spin $S_{\perp} = \sqrt{\langle \hat{S}_x \rangle^2 + \langle \hat{S}_y \rangle^2}$ and transverse off-diagonal nematic moment $Q_{\perp} = \sqrt{\langle \hat{Q}_{xz} \rangle^2 + \langle \hat{Q}_{yz} \rangle^2}$ [53], where the quadrupole operators $\hat{Q}_{ij} \equiv \hat{a}_{\alpha}^{\dagger} [S_i S_j + S_j S_i - (4/3) \delta_{ij}] \hat{a}_{\beta}$ (the indices α, β are summed over m). In the TL, the dynamics of an initial CSS is characterized by its equal-energy trajectories of the spin-nematic component on the sphere. As shown in Fig. 2(a), on the positive q side it can be tuned from that in the P' phase space (white line), separatrix dividing the BA' and P' phase space (red line linked to the unstable hyperbolic point $n_0 = 0$), and that in the BA' phase space (yellow line). Similar transitions from BA' to TF' phase can take place at $q < 0$. The spin dynamics can be denoted as coherent oscillation with varying amplitude and period, while for a CSS which is initially localized at the separatrix, it will become singular with diverging period [54].

Taking the CSS with $\{\rho_0 = 0.7, \rho_m = 0, \theta_s = \theta_m = 0\}$ as an example (whose mean-field energy \mathcal{E} is shown as the red-dashed line in Fig. 1(a)), at the intersections with the ESQPT line on $q = 0.6c$ ($\mathcal{E} = \mathcal{E}_c = E_n^c|_{N \rightarrow \infty}$), for a finite system it represents a distribution on the surface of the spin-nematic sphere with uncertainty equal to SQL ($1/\sqrt{N}$) and center located on the separatrix, which is marked as a gray circle in Fig. 2(a). Since the mean-field energy of the CSS equals that of the critical saddle point, it is closer to the eigenstate at which ESQPT takes place as compared with other higher (blue circle for $\rho_0 = 0.6$) or lower energy CSS (green circle for $\rho_0 = 0.8$), resulting in the nonanalytical features of $|c_n|^2$ at E_n^c (gray line), which are not captured by other SSSs in the P' or BA' phase (green line and blue line).

We use the CSS as the initial state to simulate QFI (2) with atom number $N = 1000$ [52] and present the dynamical behavior of $F_Q/N(ct)^2$ versus q in Fig. 2(b), where the normalization with respect to t^2 is chosen to absorb the expected long-time growth of $F_Q \propto t^2$. Around the critical points $q_c = -1.4c$ and $0.6c$, a prominent increase in the QFI can be observed, which correspond to the cases where the CSS is centered on the separatrix, linked to the saddle point $\rho_0 = 1$ and $\rho_0 = 0$, respectively. This suggests that the quantum dynamics exhibits abrupt change around the critical points and thus the QFI can serve as an indicator of ESQPTs. These two QFI peaks in the long-time limit separate the parameter space into three regions, i.e., the BA', TF', and P' phase, respectively. Apart from the phase transition region, the QFI displays damped oscillations.

Motivated by the feasibility that ESQPTs can be distinguished via the QFI, we map out the excited-state phase diagram by varying the initial CSS. One simple choice is that keep $\rho_m = 0, \theta_s = \theta_m = 0$ while vary the value of ρ_0 . For such a state the ESQPT lines display a monotonic rela-

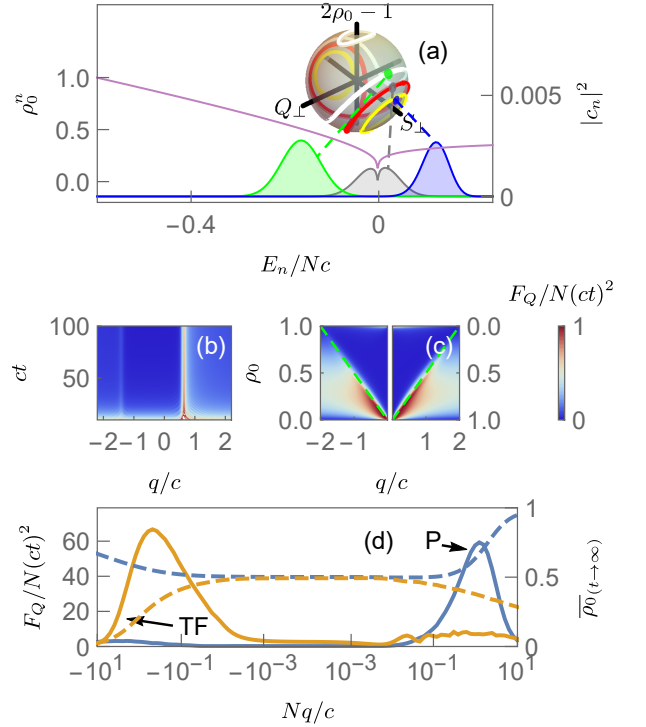


FIG. 2: (a) Slice of the phase diagram Fig. 1 at $q = 0.6c$ casted into the $\{S_{\perp}, Q_{\perp}, 2\rho_0 - 1\}$ spin-nematic sphere, where the separatrix ($\mathcal{E} = \mathcal{E}_c$, red line) separates trajectories in the BA' phase ($\mathcal{E} > \mathcal{E}_c$, yellow) from those in the P' phase ($\mathcal{E} < \mathcal{E}_c$, white), and a distribution (the blue, gray, and green circle) represents a CSS on the sphere with $\rho_0 = 0.6, 0.7, 0.8$ respectively. Eigenstate overlap $|c_n|^2$ with these CSSs are plotted (right axis), associated with the Eigenstate normalized population ρ_0^n (left axis, purple curve). (b) Time evolution of the QFI F_Q as a function of q . (c) Phase diagram in the q - ρ_0 plane computed with F_Q at $ct = 10^3$. Green-dashed curves refer to ESQPT lines. (d) F_Q calculated at $ct = 10^3$ versus q (left axis) with an initial P state (blue curve), and an initial TF state (brown curve). The corresponding dashed curves represent time-averaged population in spin-0 component $\overline{\rho_0(t)}|_{t \rightarrow \infty}$ (right axis).

tion with ρ_0 as $q_c = 2(1 - \rho_0)$ in the positive q region and $q_c = -2\rho_0$ in the negative q region. The preparation of such a CSS can be described by the formula

$$|\zeta\rangle_{\text{initial}}^{\otimes N} = \frac{1}{\sqrt{N!}} \left(e^{i\frac{\theta}{2}\hat{Q}_{yz}} \hat{a}_0^{\dagger} e^{-i\frac{\theta}{2}\hat{Q}_{yz}} \right)^N |\text{vac}\rangle, \quad (4)$$

with $\cos \theta = \sqrt{\rho_0}$ and $\sin \theta = \sqrt{1 - \rho_0}$. In experiments, Eq. (4) corresponds to a process in which one could first prepare the atoms in the $m = 0$ hyperfine state and then apply a combination of magnetic field ramps and resonant radio-frequency (rf) pulses [55] to implement polar state rotation using the quadrupole operator \hat{Q}_{yz} . Using the value of F_Q in the long time limit at $ct = 10^3$, the excited-state phase diagram is mapped out in the q - ρ_0 plane, as shown in Fig. 2(c). The vertical axis of ρ_0 is reversed in the right half ($q > 0$) with respect to the left half ($q < 0$) in order to make a comparison with the phase diagram in Fig. 1(a). The jump discontinu-

ities signaling the ESQPTs (green dashed lines) can be well captured. One can also notice that the QFI in the vicinity of $|q| = 2c$ is typically much smaller than that around $q = 0$, which can be traced to the properties of variance $\Delta\rho_0$ calculated in Fig. 1(a).

As for the DPT in ground states, the QFI in the long time limit is calculated with initial P or TF state respectively, which turns out to display a peak value at $q \simeq \pm c/N$, as shown in Fig. 2(d). These QFI peaks correspond to the QPTs of P \rightarrow S and TF \rightarrow S. For the time-averaged order parameter $\overline{\rho_0(t)}|_{t \rightarrow \infty} \equiv \lim_{T \rightarrow \infty} \frac{1}{T} \int_0^T \rho_0(t) dt = \sum_n |c_n|^2 N_0^n / N$, shown as the dashed lines, they do not display any nonanalyticity for the present small size mesoscopic quantum system.

q-estimation.—Despite that in principle the QFI can be measured via performing many-body quantum state tomography, or measure the excitation rate of a quantum state upon a periodic drive [56–58], it would be complex to implement for a quantum system of hundreds of atoms [39], and the requirement of real-time measure further prevents the feasibility of direct derivation of the QFI. In the estimation theory, the QFI sets the upper bound on the sensitivity of parameter estimation, i.e., $\Delta q \geq 1/\sqrt{F_Q(q, t)}$, which is termed as the quantum Cramér-Rao bound [49]. Thus one can get access to the estimation precision $(\Delta q)^{-2}$ through an observable \hat{O} as

$$(\Delta q)_{\hat{O}}^{-2} = \frac{|\partial_q \langle \hat{O} \rangle|^2}{\Delta^2 \hat{O}} \leq F_Q, \quad (5)$$

with $\Delta^2 \hat{O} = \langle \hat{O}^2 \rangle - \langle \hat{O} \rangle^2$ representing the variance with respect to the initial state $|\psi_0\rangle$. Eq. (5) indicates that the value of $(\Delta q)_{\hat{O}}^{-2}$ can approach F_Q with an appropriately chosen observable. SQL corresponds to $(\Delta q)_{\text{SQL}}^{-2} = Nt^2$.

Considering that optimal precision is more likely to be achieved for an observable with small variance, instead of the order parameter \hat{N}_0 , we propose to use the quadrupole operator \hat{Q}_{yz} as the observable (note that \hat{Q}_{yz} is also found to determine the best precision in a spin-1 condensate interferometry [59]). While \hat{S}_x and \hat{Q}_{yz} construct a pair of observables exhibiting spin-nematic squeezing for an initial P state [60], $\hat{S}'_x = \exp\left(i\frac{\theta}{2}\hat{Q}_{yz}\right)\hat{S}_x\exp\left(-i\frac{\theta}{2}\hat{Q}_{yz}\right)$ and \hat{Q}_{yz} are those for the CSS (4) through a unitary transformation [61]. The initial state then constitutes a minimum uncertainty state for \hat{S}'_x and \hat{Q}_{yz} , as shown in the left panel of Fig. 3(c). In experiment $Q_{yz} = \langle \hat{Q}_{yz} \rangle$ can be measured via first exchanging the distribution of Q_{yz} with that along S_x using microwave pulse, then applying a $\frac{\pi}{2}$ rf rotation about S_y and performing Stern-Gerlach gradient imaging [60]. Similar to the definition of the QFI in (2), the precision estimation also invokes an echo process, which is illustrated in Fig. 3(b). We use truncated Wigner approximation (TWA) to derive the variation of Q_{yz} after the echo [52], from which the maximum values of $(\Delta q)_{\hat{Q}_{yz}}^{-2}$ are found and they synchronize well with the behavior of F_Q , as shown in Fig. 3(a). Same as Fig. 2(b), here we also take the CSS (4) with $\rho_0 = 0.7$ as the initial state. A

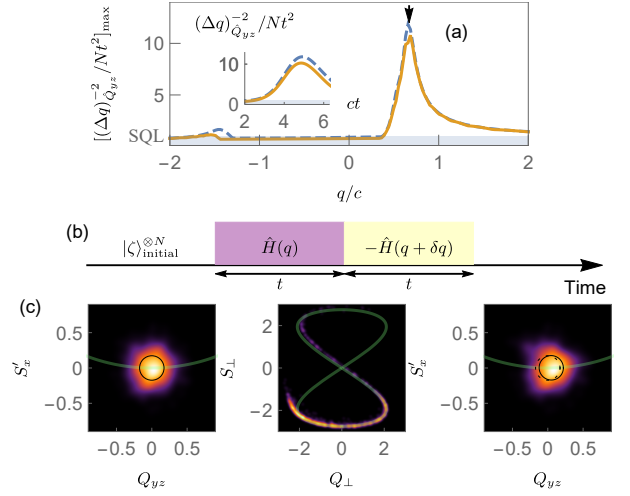


FIG. 3: (a) Maximum of the normalized estimation precision $(\Delta q)_{\hat{Q}_{yz}}^{-2}$ over time as a function of q . The arrow indicates the precision peak around $q \simeq 0.67c$, with the corresponding time evolution shown in the inset. The dashed lines are those for the QFI, which set the upper bound of the precision. (b) Schematic showing the protocol of echo for parameter estimation. (c) Density plot from the TWA simulation on the inset of (a), where time is chosen to be that the optimal precision is achieved, at $ct \simeq 4.88$. The scale is taken to be 100 atoms and the separatrix is shown in green curve. Left panel: Distribution of the initial CSS on the S'_x - Q_{yz} space with uncertainty ellipse shown in black curve. Middle panel: Distribution on the S_{\perp} - Q_{\perp} space after the time-forward propagation. Right panel: Distribution at the end of the echo. The uncertainty ellipse (black solid curve) shifts in the Q_{yz} -direction as compared with that of the initial state (black dotted curve). All calculations are for $N = 300$.

small deviation between the peaks of $(\Delta q)_{\hat{Q}_{yz}}^{-2}$ and the mean-field prediction exists, as indicated by the arrow, where the peak locates around $q \simeq 0.67c$ instead of the mean-field critical value of $q_c = 0.6c$, and this can be attributed to the transient and finite-size effects.

To understand the physics beneath the enhanced sensing, we explore the echo process during which $(\Delta q)_{\hat{Q}_{yz}}^{-2}$ reaches its peak value (the inset of Fig. 3(a)). After a time-forward evolution under $\hat{H}(q)$, the atomic state is dispersed along the separatrix, with its majority surpassing the saddle point, as shown in the middle panel of Fig. 3(c). Noticeably that part of the quasi-probability distribution even leaves the separatrix and enters into the P' phase space. This is due to that the motion near the separatrix is apt to phase space mixing [62]. At the end of the echo after experiencing a time-reversing evolution under $\hat{H}(q + \delta q)$, the state approximately recovers the initial CSS (right panel of Fig. 3(c)), with a small shift in the Q_{yz} component (compare the uncertainty ellipse of initial and final states, marked by dotted and solid line respectively). A small perturbation in the control parameter ($\delta q = 10^{-3}c$ in Fig. 3(c)) can give rise to non-negligible variation in the observable, and this roots in the sensitive dependence of quantum state evolution upon the deformation of the separatrix, which is well captured through an echo process near the criti-

cal points.

Conclusion.—In summary, we have shown the existence of QPTs and ESQPTs in an antiferromagnetic spin-1 condensate and demonstrated their correspondence with DPT, which is characterized using the QFI. We propose that DPT with the condensate initially prepared in an CSS can be used to probe the quantum criticality in excited states, which gives rise to a peak value of the QFI. It can also be used to implement sub-SQL estimation on the effective quadratic Zeeman energy q . This extends the precise estimation of the critical q_c to a much wider parameter region beyond those at which ground state QPTs take place [63, 64]. It is interesting to note that the ground-state phase transitions from symmetry-broken states to the symmetry-restored spin-singlet state can also be indicated by the DPT. Though we have focused on the system of spinor condensate, the method of exploring ESQPTs presented here can be applied to a broad class of few-mode quantum systems.

Acknowledgements.—We thank Han Pu for careful reading on the manuscript and Keye Zhang for useful discussions. This work is supported by the Innovation Program for Quantum Science and Technology (2021ZD0303200); National Key Research and Development Program of China (Grant No. 2016YFA0302001), the National Natural Science Foundation of China (Grant Nos. 12074120, 11374003, 11654005, 12234014, 12005049, 11935012), the Shanghai Municipal Science and Technology Major Project (Grant No. 2019SHZDZX01), and the Fundamental Research Funds for the Central Universities. W.Z. acknowledges additional support from the Shanghai Talent Program.

* Electronic address: lzhou@phy.ecnu.edu.cn

† Electronic address: z.lan@ucl.ac.uk

‡ Electronic address: wpz@sju.edu.cn

- [1] S. Sachdev, *Quantum Phase Transitions* (Cambridge University Press, 2000).
- [2] P. Cejnar, P. Stránský, M. Macek, and M. Kloc, *Journal of Physics A: Mathematical and Theoretical* **54**, 133001 (2021).
- [3] P. Cejnar, M. Macek, S. Heinze, J. Jolie, and J. Dobeš, *Journal of Physics A: Mathematical and General* **39**, L515 (2006).
- [4] M. Caprio, P. Cejnar, and F. Iachello, *Annals of Physics* **323**, 1106 (2008).
- [5] A. L. Corps and A. Relaño, *Phys. Rev. Lett.* **127**, 130602 (2021).
- [6] H. Lipkin, N. Meshkov, and A. Glick, *Nuclear Physics* **62**, 188 (1965).
- [7] V. Ulyanov and O. Zaslavskii, *Physics Reports* **216**, 179 (1992).
- [8] M. Heyl, A. Polkovnikov, and S. Kehrein, *Phys. Rev. Lett.* **110**, 135704 (2013).
- [9] M. Heyl, *Phys. Rev. Lett.* **115**, 140602 (2015).
- [10] M. Heyl, *EPL (Europhysics Letters)* **125**, 26001 (2019).
- [11] S. De Nicola, A. A. Michailidis, and M. Serbyn, *Phys. Rev. Lett.* **126**, 040602 (2021).
- [12] S. Vajna and B. Dóra, *Phys. Rev. B* **91**, 155127 (2015).
- [13] P. Jurcevic, H. Shen, P. Hauke, C. Maier, T. Brydges, C. Hempel, B. P. Lanyon, M. Heyl, R. Blatt, and C. F. Roos, *Phys. Rev. Lett.* **119**, 080501 (2017).
- [14] K. Yang, L. Zhou, W. Ma, X. Kong, P. Wang, X. Qin, X. Rong, Y. Wang, F. Shi, J. Gong, and J. Du, *Phys. Rev. B* **100**, 085308 (2019).
- [15] X.-Y. Guo, C. Yang, Y. Zeng, Y. Peng, H.-K. Li, H. Deng, Y.-R. Jin, S. Chen, D. Zheng, and H. Fan, *Phys. Rev. Applied* **11**, 044080 (2019).
- [16] J. Lang, B. Frank, and J. C. Halimeh, *Phys. Rev. Lett.* **121**, 130603 (2018).
- [17] N. Fläschner, D. Vogel, M. Tarnowski, B. S. Rem, D. S. Lühmann, M. Heyl, J. C. Budich, L. Mathey, K. Sengstock, and C. Weitenberg, *Nature Physics* **14**, 265 (2018).
- [18] J. Zhang, G. Pagano, P. W. Hess, A. Kyprianidis, P. Becker, H. Kaplan, A. V. Gorshkov, Z. X. Gong, and C. Monroe, *Nature* **551**, 601 (2017).
- [19] J. A. Muniz, D. Barberena, R. J. Lewis-Swan, D. J. Young, J. R. Cline, A. M. Rey, and J. K. Thompson, *Nature* **580**, 602 (2020).
- [20] T.-L. Ho and S. K. Yip, *Phys. Rev. Lett.* **84**, 4031 (2000).
- [21] Y. Kawaguchi and M. Ueda, *Physics Reports* **520**, 253 (2012).
- [22] D. M. Stamper-Kurn and M. Ueda, *Rev. Mod. Phys.* **85**, 1191 (2013).
- [23] L. Sadler, J. Higbie, S. Leslie, M. Vengalattore, and D. Stamper-Kurn, *Nature* **443**, 312 (2006).
- [24] J. Jiang, L. Zhao, M. Webb, and Y. Liu, *Phys. Rev. A* **90**, 023610 (2014).
- [25] H.-X. Yang, T. Tian, Y.-B. Yang, L.-Y. Qiu, H.-Y. Liang, A.-J. Chu, C. B. Dağ, Y. Xu, Y. Liu, and L.-M. Duan, *Phys. Rev. A* **100**, 013622 (2019).
- [26] E. M. Bookjans, A. Vinit, and C. Raman, *Phys. Rev. Lett.* **107**, 195306 (2011).
- [27] L. A. Williamson and P. B. Blakie, *Phys. Rev. Lett.* **116**, 025301 (2016).
- [28] M. Uhlmann, R. Schützhold, and U. R. Fischer, *Phys. Rev. Lett.* **99**, 120407 (2007).
- [29] B. Damski and W. H. Zurek, *Phys. Rev. Lett.* **99**, 130402 (2007).
- [30] L.-Y. Qiu, H.-Y. Liang, Y.-B. Yang, H.-X. Yang, T. Tian, Y. Xu, and L.-M. Duan, *Science Advances* **6**, eaba7292 (2020).
- [31] X.-Y. Luo, Y.-Q. Zou, L.-N. Wu, Q. Liu, M.-F. Han, M. K. Tey, and L. You, *Science* **355**, 620 (2017).
- [32] Y.-Q. Zou, L.-N. Wu, Q. Liu, X.-Y. Luo, S.-F. Guo, J.-H. Cao, M. K. Tey, and L. You, *Proceedings of the National Academy of Sciences* **115**, 6381 (2018).
- [33] C. B. Dağ, S.-T. Wang, and L.-M. Duan, *Phys. Rev. A* **97**, 023603 (2018).
- [34] T. Tian, H.-X. Yang, L.-Y. Qiu, H.-Y. Liang, Y.-B. Yang, Y. Xu, and L.-M. Duan, *Phys. Rev. Lett.* **124**, 043001 (2020).
- [35] P. Feldmann, C. Klempt, A. Smerzi, L. Santos, and M. Gessner, *Phys. Rev. Lett.* **126**, 230602 (2021).
- [36] J. Cabedo, J. Claramunt, and A. Celi, *Phys. Rev. A* **104**, L031305 (2021).
- [37] J. Cabedo and A. Celi, *Phys. Rev. Research* **3**, 043215 (2021).
- [38] L. Zhao, J. Jiang, T. Tang, M. Webb, and Y. Liu, *Phys. Rev. A* **89**, 023608 (2014).
- [39] B. Evrard, A. Qu, J. Dalibard, and F. Gerbier, *Science* **373**, 1340 (2021).
- [40] C. K. Law, H. Pu, and N. P. Bigelow, *Phys. Rev. Lett.* **81**, 5257 (1998).
- [41] S. Peotta, F. Brange, A. Deger, T. Ojanen, and C. Flindt, *Phys. Rev. X* **11**, 041018 (2021).
- [42] T. Gorin, T. Prosen, T. H. Seligman, and M. Žnidarič, *Physics Reports* **435**, 33 (2006).
- [43] P. Pérez-Fernández, A. Relaño, J. M. Arias, J. Dukelsky, and J. E. García-Ramos, *Phys. Rev. A* **80**, 032111 (2009).

- [44] A. Relaño, J. M. Arias, J. Dukelsky, J. E. García-Ramos, and P. Pérez-Fernández, *Phys. Rev. A* **78**, 060102 (2008).
- [45] T. Macrì, A. Smerzi, and L. Pezzè, *Phys. Rev. A* **94**, 010102 (2016).
- [46] F. Gerbier, A. Widera, S. Fölling, O. Mandel, and I. Bloch, *Phys. Rev. A* **73**, 041602 (2006).
- [47] S. R. Leslie, J. Guzman, M. Vengalattore, J. D. Sau, M. L. Cohen, and D. M. Stamper-Kurn, *Phys. Rev. A* **79**, 043631 (2009).
- [48] K. Murata, H. Saito, and M. Ueda, *Phys. Rev. A* **75**, 013607 (2007).
- [49] S. L. Braunstein and C. M. Caves, *Phys. Rev. Lett.* **72**, 3439 (1994).
- [50] S. Pang and T. A. Brun, *Phys. Rev. A* **90**, 022117 (2014).
- [51] Q. Guan and R. J. Lewis-Swan, *Phys. Rev. Research* **3**, 033199 (2021).
- [52] See supplemental material for details about numerical methods, secular approximation of the QFI, and experimental perspectives.
- [53] T. M. Hoang, C. S. Gerving, B. J. Land, M. Anquez, C. D. Hamley, and M. S. Chapman, *Phys. Rev. Lett.* **111**, 090403 (2013).
- [54] W. Zhang, D. L. Zhou, M.-S. Chang, M. S. Chapman, and L. You, *Phys. Rev. A* **72**, 013602 (2005).
- [55] B. Evrard, A. Qu, J. Dalibard, and F. Gerbier, *Phys. Rev. A* **103**, L031302 (2021).
- [56] T. Ozawa and N. Goldman, *Phys. Rev. B* **97**, 201117 (2018).
- [57] T. Ozawa and N. Goldman, *Phys. Rev. Research* **1**, 032019 (2019).
- [58] M. Yu, Y. Liu, P. Yang, M. Gong, Q. Cao, S. Zhang, H. Liu, M. Heyl, T. Ozawa, N. Goldman, and J. Cai, *npj Quantum Information* **8** (2022), 10.1038/s41534-022-00547-x.
- [59] A. Niezgodą, D. Kajtoch, J. Dziekańska, and E. Witkowska, *New Journal of Physics* **21**, 093037 (2019).
- [60] C. D. Hamley, C. Gerving, T. Hoang, E. Bookjans, and M. S. Chapman, *Nature Physics* **8**, 305 (2012).
- [61] E. Yukawa, M. Ueda, and K. Nemoto, *Phys. Rev. A* **88**, 033629 (2013).
- [62] R. Mathew and E. Tiesinga, *Phys. Rev. A* **96**, 013604 (2017).
- [63] S. S. Mirkhalaf, E. Witkowska, and L. Lepori, *Phys. Rev. A* **101**, 043609 (2020).
- [64] S. S. Mirkhalaf, D. Benedicto Orenes, M. W. Mitchell, and E. Witkowska, *Phys. Rev. A* **103**, 023317 (2021).

Supplemental Materials: Dynamical quantum phase transitions in a spinor Bose-Einstein condensate and criticality enhanced quantum sensing

I. NUMERICAL METHODS

We solve the time evolution of quantum states using the exact diagonalization method. The initial state of the system is described by a coherent spin state $|\zeta\rangle^{\otimes N}$ with (assuming $\rho_{+1} = \rho_{-1}$)

$$\zeta = \begin{pmatrix} \zeta_{+1} \\ \zeta_0 \\ \zeta_{-1} \end{pmatrix} = \begin{pmatrix} \sqrt{\frac{1-\rho_0}{2}} e^{i\phi_{+1}} \\ \sqrt{\rho_0} e^{i\phi_0} \\ \sqrt{\frac{1-\rho_0}{2}} e^{i\phi_{-1}} \end{pmatrix}, \quad (\text{S1})$$

where equal population in the spin- ± 1 sublevels is assumed. $|\zeta\rangle^{\otimes N}$ can be written in the Fock basis as

$$|\zeta\rangle^{\otimes N} = \frac{1}{\sqrt{N!}} \left(\zeta_{+1} \hat{a}_{+1}^\dagger + \zeta_0 \hat{a}_0^\dagger + \zeta_{-1} \hat{a}_{-1}^\dagger \right)^N |0\rangle, \quad (\text{S2})$$

which can be expanded in the Fock basis $|N_0, M\rangle \equiv |N_1 = \frac{N-N_0+M}{2}, N_0, N_{-1} = \frac{N-N_0-M}{2}\rangle$ as $|\zeta\rangle^{\otimes N} = \sum_{N_0, M} f(N_0, M) |N_0, M\rangle$ with the coefficient

$$f(N_0, M) = \sqrt{\frac{N!}{N_1! N_0! N_{-1}!}} \left(\sqrt{\frac{1-\rho_0}{2}} \right)^{N-N_0} (\sqrt{\rho_0})^{N_0} \exp[i(N_1 \phi_{+1} + N_0 \phi_0 + N_{-1} \phi_{-1})]. \quad (\text{S3})$$

Due to the presence of the SO(2) symmetry in the Hamiltonian (1) [S1], the generator \hat{S}_z is conserved, i.e., the magnetization M is a conserved quantity. Then the Hamiltonian matrix \hat{H} written in the $|N_0, M\rangle$ basis is block diagonal, for which there are $2N+1$ blocks with the value of M running from $-N$ to N and each block has a dimension $\left[\frac{N-M}{2} + 1\right] \times \left[\frac{N-M}{2} + 1\right]$ (here $[\cdot]$ means taking the integer part). Each block matrix is tridiagonal and can be diagonalized separately, then the time evolved state $|\psi(q, t)\rangle$ can be computed.

Some spin operators such as \hat{Q}_{yz} couples blocks of different M , which makes its matrix size very large and inconvenient to perform simulation. We adopt TWA to study its dynamics [S2–S5]. TWA states that the Wigner function W for a quantum state approximately follows the equation

$$i\hbar \frac{\partial W}{\partial t} \simeq \{H_W, W\}_C, \quad (\text{S4})$$

where H_W is the Wigner-Weyl transform of the Hamiltonian, and $\{\cdot\cdot\}_C$ is the coherent state Poisson bracket. Similarly in the coherent state picture we treat the operators \hat{a}_j (\hat{a}_j^\dagger) as complex c -numbers α_j (α_j^*), and making Wigner-Weyl transform to the Heisenberg equations we have

$$i\hbar \frac{\partial \alpha_j}{\partial t} \simeq \{\alpha_j, H_W\}_C = \frac{\partial H_W}{\partial \alpha_j^*}. \quad (\text{S5})$$

TWA then invokes first sampling the Wigner distribution W with many sets of $\{\alpha_j, \alpha_j^*\}$, and then for each set we solve the equation of motion (S5). Any observable of interest is obtained from the ensemble average. To sample $|\zeta\rangle^{\otimes N}$, we first sample the polar state $\frac{1}{\sqrt{N!}} \hat{a}_0^{\dagger N} |\text{vac}\rangle$ with

$$\begin{pmatrix} \alpha_1 \\ \alpha_0 \\ \alpha_{-1} \end{pmatrix} = \begin{pmatrix} (a+ib)/2 \\ (e+f\eta) e^{i2\pi\xi} \\ (c+id)/2 \end{pmatrix}, \quad (\text{S6})$$

where a, b, c, d, η are independent random numbers drawn from Gaussian distribution with zero mean and unit variance, while ξ is a random number drawn from uniform distribution in $[0, 1]$, and [S6]

$$e = \frac{1}{2} \sqrt{2N+1 + 2\sqrt{N^2+N}}, f = \frac{1}{4e}. \quad (\text{S7})$$

Unitary transformation (4) is equivalent to performing the rotation

$$\begin{pmatrix} \frac{\cos \theta + 1}{2} & \frac{\sin \theta}{\sqrt{2}} & \frac{\cos \theta - 1}{2} \\ -\frac{\sin \theta}{\sqrt{2}} & \cos \theta & -\frac{\sin \theta}{\sqrt{2}} \\ \frac{\cos \theta - 1}{2} & \frac{\sin \theta}{\sqrt{2}} & \frac{\cos \theta + 1}{2} \end{pmatrix} \begin{pmatrix} \alpha_1 \\ \alpha_0 \\ \alpha_{-1} \end{pmatrix}. \quad (\text{S8})$$

We sample a system of $N = 300$ with 1000 trajectories. It has been compared with the exact quantum mechanical calculations regarding the expectation values and variances of different spin operators, where good agreements are found. TWA is capable to simulate quantum dynamics in short time scale, which is enough for us to produce Fig. 3. However it will deviate significantly from the exact quantum mechanical calculations when the evolution time becomes large, due to the omitted high-order terms.

II. SECULAR APPROXIMATION OF THE QFI

The QFI (2) can be written in a tensor form as [S7]

$$F_Q(q, t) = 4 \left(\langle \partial_q \psi | \partial_q \psi \rangle - |\langle \psi | \partial_q \psi \rangle|^2 \right), \quad (\text{S9})$$

where $|\psi\rangle = |\psi(q, t)\rangle = e^{-i\hat{H}t} |\psi_0\rangle$. If $\hat{H} = q\hat{H}_q$, one can immediately realize that $F_Q(q, t) = 4t^2 \Delta^2 \hat{H}_q$ with the variance $\Delta^2 \hat{H}_q = \langle \psi_0 | \hat{H}_q^2 | \psi_0 \rangle - \left| \langle \psi_0 | \hat{H}_q | \psi_0 \rangle \right|^2$. Recognizing $\hat{H} = \hat{H}_0 + q\hat{H}_q$ and $[\hat{H}_0, \hat{H}_q] \neq 0$, we use the identity [S8]

$$\exp(i\hat{H}t) \frac{\partial}{\partial q} \exp(-i\hat{H}t) = -i \int_0^t dt' \exp(i\hat{H}t') \frac{\partial \hat{H}}{\partial q} \exp(-i\hat{H}t') = -i\hat{\mathcal{H}}_q, \quad (\text{S10})$$

where $\hat{\mathcal{H}}_q = \int_0^t dt' \exp(i\hat{H}t') \hat{H}_q \exp(-i\hat{H}t')$ and this leads to $F_Q(q, t) = 4\Delta^2 \hat{\mathcal{H}}_q$. Usually, it is not easy to work out the explicit form of $\hat{\mathcal{H}}_q$ except that the Hamiltonian belongs to some special classes [S9]. Using the expansion $|\psi_0\rangle = \sum_n c_n |\psi_n\rangle$, in which $|\psi_n\rangle$ is the eigenstate of \hat{H} with the corresponding eigenenergy E_n , we can get

$$F_Q(q, t) = 4t^2 \left[\sum_n \left| \sum_m c_m H_q^{nm} \text{sinc}\left(\frac{E_{nm}t}{2}\right) e^{iE_{nm}t/2} \right|^2 - \left| \sum_{n,m} c_n^* c_m H_q^{nm} \text{sinc}\left(\frac{E_{nm}t}{2}\right) e^{iE_{nm}t/2} \right|^2 \right], \quad (\text{S11})$$

where $E_{nm} = E_n - E_m$. In the long-time limit, the sinc function gives the value of 1 with $E_{nm} = 0$ and zero otherwise. Using an assumption that only the terms with $E_{nm} = 0$ survive in the $t \rightarrow \infty$ limit [S10] and considering the fact that the spectrum of \hat{H} is nondegenerate, the QFI (S11) can be approximated by Eq. (3) in the main text.

We found out that the approximation is quantitatively valid in a moderate long time. From the viewpoint of phase space mixing [S11], a distribution in phase space will eventually mix up in the energy region it could reach, which will reduce its distinguishability. The sensitivity of a quantum state with respect to the change of Hamiltonian parameters, as characterized by the QFI, is also expected to become coarse in the long-time run.

III. EXPERIMENTAL CONSIDERATION

The echo including first evolves an initial state $|\psi_0\rangle$ forward with $\hat{H}(q)$ and then backward with $\hat{H}(q + \delta q)$. To implement this, one needs to reverse the sign of the Hamiltonian $\hat{H} = \hat{H}_0 + q\hat{H}_q$ such that the system can experience time-reversing evolution. In experiments, the sign of the control parameter q can be varied via microwave dressing [S12–S14]. On the other hand, the sign of \hat{H}_0 is determined by the spin-dependent interaction coefficient c , which may be reversed via transferring the atoms from the $F = 1$ hyperfine manifold to that of $F = 2$ [S15]. Another promising technique could be exploited is the photon-mediated spin-exchange interactions, which was experimentally realized recently with the aid of a cavity light field [S16, S17]. Other methods capable of manipulating spin-dependent collision interactions, such as photoassociation [S18], also exist.

* Electronic address: lzhou@phy.ecnu.edu.cn

† Electronic address: z.lan@ucl.ac.uk

‡ Electronic address: wpz@sjtu.edu.cn

- [S1] Y. Kawaguchi and M. Ueda, Symmetry classification of spinor Bose-Einstein condensates, *Phys. Rev. A* **84**, 053616 (2011).
- [S2] P. B. Blakie, A. S. Bradley, M. J. Davis, R. J. Ballagh, and C. W. Gardiner, Dynamics and statistical mechanics of ultra-cold Bose gases using c-field techniques, *Adv. Phys.* **57**, 363 (2008).
- [S3] A. Polkovnikov, Phase space representation of quantum dynamics, *Ann. Phys.* **325**, 1790 (2010).
- [S4] J. Schachenmayer, A. Pikovski, and A. M. Rey, Many-Body Quantum Spin Dynamics with Monte Carlo Trajectories on a Discrete Phase Space, *Phys. Rev. X* **5**, 011022 (2015).
- [S5] A. Sinatra, C. Lobo and Y. Castin, The truncated Wigner method for Bose-condensed gases: limits of validity and applications, *J. Phys. B* **35**, 3599 (2002).
- [S6] M. K. Olsen and A. S. Bradley, Numerical representation of quantum states in the positive- P and Wigner representations, *Opt. Comm.* **282**, 3924 (2009).
- [S7] L. C. Venuti and P. Zanardi, Quantum Critical Scaling of the Geometric Tensors, *Phys. Rev. Lett.* **99**, 095701 (2007).
- [S8] R. M. Wilcox, Exponential Operators and Parameter Differentiation in Quantum Physics, *J. Math. Phys.* **8**, 962 (1967).
- [S9] Y. Chu, S. Zhang, B. Yu, and J. Cai, Dynamic Framework for Criticality-Enhanced Quantum Sensing, *Phys. Rev. Lett.* **126**, 010502 (2021).
- [S10] Q. Guan and R. J. Lewis-Swan, Identifying and harnessing dynamical phase transitions for quantum-enhanced sensing, *Phys. Rev. Research* **3**, 033199 (2021).
- [S11] R. Mathew and E. Tiesinga, Phase-space mixing in dynamically unstable, integrable few-mode quantum systems, *Phys. Rev. A* **96**, 013604 (2017).
- [S12] P. Kunkel, M. Prüfer, H. Strobel, D. Linnemann, A. Frölian, T. Gasenzer, M. Gärtner, and M. K. Oberthaler, Spatially distributed multipartite entanglement enables EPR steering of atomic clouds, *Science* **360**, 413 (2018).
- [S13] F. Gerbier, A. Widera, S. Fölling, O. Mandel, and I. Bloch, Resonant control of spin dynamics in ultracold quantum gases by microwave dressing, *Phys. Rev. A* **73**, 041602 (2006).
- [S14] S. R. Leslie, J. Guzman, M. Vengalattore, J. D. Sau, M. L. Cohen, and D. M. Stamper-Kurn, Amplification of fluctuations in a spinor Bose-Einstein condensate, *Phys. Rev. A* **79**, 043631 (2009).
- [S15] P. Kunkel, M. Prüfer, S. Lannig, R. Rosa-Medina, A. Bonnini, M. Gärtner, H. Strobel, and M. K. Oberthaler, Simultaneous Readout of Noncommuting Collective Spin Observables beyond the Standard Quantum Limit, *Phys. Rev. Lett.* **123**, 063603 (2019).
- [S16] E. J. Davis, G. Bentsen, L. Homeier, T. Li, and M. H. Schleier-Smith, Photon-Mediated Spin-Exchange Dynamics of Spin-1 Atoms, *Phys. Rev. Lett.* **122**, 010405 (2019).
- [S17] M. A. Norcia, R. J. Lewis-Swan, J. R. K. Cline, B. Zhu, A. M. Rey, and J. K. Thompson, Cavity-mediated collective spin-exchange interactions in a strontium superradiant laser, *Science* **361**, 259 (2018).
- [S18] H. Jing, Y. Jiang, W. Zhang, and P. Meystre, Laser-catalyzed spin-exchange process in a Bose-Einstein condensate, *Phys. Rev. A* **81**, 031603 (2010).